Geophysical Research Letters®

RESEARCH LETTER

10.1029/2024GL112798

Statistical Relationship Between Electron Flux and Resonant Chorus Wave Power Near the Flux Limit

Emile Saint-Girons[1,2], **Xiao-Jia Zhang**[1,3], **Didier Mourenas**[4,5], **Anton V. Artemyev**[3], and **Vassilis Angelopoulos**[3]

[1]Department of Physics, University of Texas at Dallas, Richardson, TX, USA, [2]CentraleSupélec, Gif-sur-Yvette, France, [3]Department of Earth, Planetary, and Space Sciences, University of California, Los Angeles, Los Angeles, CA, USA, [4]CEA, DAM, DIF, Arpajon, France, [5]Laboratoire Matière en Conditions Extrêmes, Université Paris-Saclay, CEA, Bruyères-le-Châtel, France

Key Points:

- We statistically analyze the saturation of radiation belt electron flux, using low-altitude pitch-angle resolved electron flux measurements
- The inferred resonant chorus wave power gain increases proportionally to theoretical linear wave power gain for moderately high linear gain
- The average amplitudes of resonant chorus waves exhibit saturation, resulting in a soft limitation of electron fluxes

Correspondence to:

X.-J. Zhang,
xjzhang@utdallas.edu

Citation:

Saint-Girons, E., Zhang, X.-J., Mourenas, D., Artemyev, A. V., & Angelopoulos, V. (2024). Statistical relationship between electron flux and resonant chorus wave power near the flux limit. *Geophysical Research Letters*, *51*, e2024GL112798. https://doi.org/10.1029/2024GL112798

Received 26 SEP 2024
Accepted 4 NOV 2024

Abstract Electron precipitation by chorus whistler-mode waves generated by the same electron population is expected to play an important role in the dynamics of the outer radiation belt, potentially setting a hard upper limit on trapped energetic electron fluxes. Here, we statistically analyze the relationship between equatorial electron fluxes and the power of mid-latitude cyclotron-resonant chorus waves precipitating these electrons, both inferred from ELFIN low-altitude energy and pitch-angle resolved electron flux measurements in 2020–2022. We provide clear evidence of a flux limitation coinciding with an exponential increase of precipitation. We statistically demonstrate that the actual inferred resonant wave power gains are well correlated with theoretical linear gains, as in the classical Kennel-Petschek model, for moderately high linear gains and high fluxes. However, we also find a finite occurrence of very high fluxes, corresponding to resonant waves of moderate average amplitude, implying a softer, more dynamical upper limit than traditionally envisioned.

Plain Language Summary Using high-precision spacecraft measurements of electron fluxes at low altitude, we experimentally revisit the classical Kennel-Petschek paradigm of electron flux self limitation in the Earth's outer radiation belt. Our statistical analysis demonstrates that, above a threshold, higher electron fluxes are associated with the generation of more intense electromagnetic waves, which scatter electrons more efficiently toward the atmosphere, where they are lost. This leads to a lower occurrence of higher fluxes. Furthermore, we find that wave intensity increases as predicted by theory. While these results confirm the classical notion of an upper limit on electron fluxes, we discover that this limit is softer and more gradual than previously expected. This is probably due to an unforeseen saturation of the wave intensity that reduces the flux-limiting effects of these waves during a sufficiently strong increase of electron fluxes.

1. Introduction

Electron precipitation into the atmosphere, through pitch-angle diffusion by whistler-mode chorus waves, is a key mechanism for the loss of energetic electrons from the Earth's outer radiation belt (Agapitov et al., 2018; Chakraborty et al., 2022; Kasahara et al., 2019; Thorne et al., 2005). Chorus waves are generated outside the plasmasphere, in the form of rising tone elements, by trapped energetic electrons injected during substorms, and reach a higher intensity during higher geomagnetic activity (Agapitov et al., 2018; Chakraborty et al., 2022; Fu et al., 2014; Meredith et al., 2020; Omura et al., 2008; Tsurutani & Smith, 1977). Consequently, an important question arises regarding the efficiency of electron precipitation driven by these waves in limiting the trapped electron fluxes that generate them (Hua, Bortnik, & Ma, 2022; Kennel & Petschek, 1966; Mauk & Fox, 2010; Mourenas et al., 2023, 2024; Olifer et al., 2022; Ozeke et al., 2024; Summers et al., 2009).

The Kennel-Petschek model of flux self-limitation postulates that whistler-mode waves of exponentially increasing power are generated as the equatorial omnidirectional trapped electron flux $J_{omni,eq}$ rises (Kennel & Petschek, 1966). This leads to an exponentially faster electron precipitation into the atmosphere through pitch-angle diffusion, while wave-driven energy diffusion is assumed to be negligible (Kennel & Petschek, 1966). This sets an upper limit, $J^{KP}_{omni,eq}$, on the trapped flux (Kennel & Petschek, 1966). The Kennel-Petschek limit $J^{KP}_{omni,eq}$ was initially assumed to correspond to a maximum theoretical linear wave power gain $G_{th,\max} = \int (2\gamma/v_g)\,dz \approx 6$ along magnetic field lines (with γ the parallel wave linear growth rate, v_g its group speed, z the field line coordinate). This maximum gain, $G_{th,\max} \approx 6$, was deemed sufficient for ensuring a balance between low-latitude wave generation and high-latitude wave loss, based on an assumed high-latitude reflection of ≈0.25% of the wave power (Kennel & Petschek, 1966). Schulz and Davidson (1988) later revised this estimate to $G_{th,\max} = 3$, a value adopted in subsequent works (Mauk & Fox, 2010; Olifer et al., 2022; Summers et al., 2009). However, Summers et al. (2009) noted that chorus wave growth from the observed noise level might require $G_{\max} \approx 6 - 12$ (in agreement with Carlson et al., 1985).

In the case of chorus waves, however, electron energy diffusion is not negligible compared with pitch-angle diffusion (Horne et al., 2005). Then, a second, more dynamical upper limit, $J^{up}_{omni,eq}$, which represents an attractor for the system dynamics, may be reached when the number of precipitated electrons per second at each energy balances the number of electrons injected or accelerated to this energy per second (Hua, Bortnik, & Ma, 2022; Mourenas, Artemyev, et al., 2022; Mourenas et al., 2023; Summers & Stone, 2022).

In this study, we utilize energy and pitch-angle resolved measurements of electron fluxes from the Electron Losses and Fields Investigation (ELFIN) CubeSats, which operate in a nearly polar Low Earth Orbit (Angelopoulos et al., 2020, 2023). We investigate how the precipitating-to-trapped flux ratio and the chorus wave power at cyclotron resonance with electrons near the loss cone, vary with $J_{omni,eq}$ and linear wave power gain at high $J_{omni,eq}$. A key advantage of using ELFIN measurements (rather than measurements from an equatorial spacecraft) is that, as will be shown in Section 2, these quantities can be simultaneously inferred from the same data set. This ensures consistency between all inferred quantities, a crucial point for our statistical study of flux self-limitation, performed in Section 3.

2. Inferring Equatorial Electron Flux and Resonant Wave Power From ELFIN Low-Altitude Measurements

ELFIN measurements of precipitating, trapped, and backscattered electron fluxes at ∼450 km altitude in 2020–2022 are used to infer omnidirectional equatorial electron fluxes $J_{omni,eq}$ at different energies. The trapped electron flux, J_{trap}, is measured by ELFIN just above the bounce loss cone. We calculate the effective net precipitating flux, $J_{prec,eff}$, caused by chorus waves, as the difference between the measured precipitating flux averaged inside the local bounce loss cone and the mean upward flux backscattered by the atmosphere within the same loss cone (Mourenas et al., 2021, 2023). This calculation assumes that most backscattered electrons remain within a given energy bin of width $\Delta E/E \approx 40\%$ (Marshall & Bortnik, 2018; Selesnick et al., 2004), and that the system is roughly symmetric with respect to the magnetic equator.

We focus on periods of significant geomagnetic activity, parameterized by the auroral SuperMAG *SME* index (Gjerloev, 2012), at $L = 4.5 \pm 0.25$ in the 3–9 MLT sector. In this region, intense chorus waves are present up to magnetic latitudes $\lambda > 25°$, allowing efficient wave-driven $60 - 500$ keV electron precipitation (Agapitov et al., 2018). To obtain a large statistical ensemble, we collect all ELFIN measurements in 2020–2022 that were preceded by a high time-integrated *SME*, $Int(SME) \approx (2 - 3) \times 10^4$ nT·hr, calculated over 72 hr. This elevated time-integrated activity correlates with maximum $100 - 3000$ keV electron fluxes near $L = 4.5$ (Hua & Bortnik, 2024; Hua, Bortnik, Chu, et al., 2022; Mourenas, Agapitov, et al., 2022; Mourenas et al., 2019). Typically, it corresponds to peaks of 1-min *SME* above $\sim 800 - 1000$ nT, suggesting that the measurements likely occurred outside the plasmasphere (Agapitov et al., 2019; Hua & Bortnik, 2024; O'Brien & Moldwin, 2003).

We assume a nearly diffusive transport of electrons through resonant interactions with mainly short chorus wave packets separated by random phase jumps (Artemyev et al., 2021, 2022; Mourenas, Zhang, et al., 2022; Zhang et al., 2020). Additionally, we consider a quasi-equilibrium pitch-angle distribution at $0.06 - 0.5$ MeV after hours to days of wave-particle interactions (as justified by previous works, see Mourenas et al., 2021; Shane et al., 2023). In this case, the quasi-linear diffusion theory (Kennel & Petschek, 1966) indicates that the wave-driven electron pitch-angle diffusion rate near the loss cone can be expressed as follows:

$$D_{\alpha\alpha} = \frac{4\ \alpha^2_{eq,LC}}{z_0^2\ \ \tau_B}, \tag{1}$$

with $\alpha_{eq,LC}$ the equatorial bounce loss-cone angle, τ_B the electron bounce period, and z_0 a function of the average flux ratio $J_{prec,eff}/J_{trap}$. z_0 is given by the approximate relationship:

$$z_0 \simeq \left(10^4 + 260\,\frac{J_{trap}}{J_{prec,eff}}\right)^{1/2} - 100, \tag{2}$$

valid for $J_{prec,eff}/J_{trap} = 0.001 - 0.85$ with less than ∼25% error (Mourenas et al., 2023, 2024).

The quasi-equilibrium directional electron flux at the equator, $J(\alpha_{eq})$, is then given by (Kennel & Petschek, 1966; Mourenas et al., 2023):

$$\frac{J(\alpha_{eq})}{J_{trap}} \approx \frac{1 + z_0\frac{I_1(z_0)}{I_0(z_0)}\ln\left(\frac{\sin\alpha_{eq}}{\sin\alpha_{eq,LC}}\right)}{1 + z_0\frac{I_1(z_0)}{I_0(z_0)}\ln\left(\frac{\sin\alpha_{eq,trap}}{\sin\alpha_{eq,LC}}\right)}, \tag{3}$$

with I_x the modified Bessel function of the first kind and $\alpha_{eq,trap} \simeq 1.05\ \alpha_{eq,LC}$. Using Equations 2 and 3, we can deduce the directional flux $J(\alpha_{eq})$ and, after integration over α_{eq}, the equatorial omnidirectional electron flux $J_{omni,eq}$, from $J_{prec,eff}/J_{trap}$ and J_{trap} measured by ELFIN. When $J_{prec,eff}/J_{trap} > 0.85$, however, we reach the strong diffusion regime (Kennel, 1969; Lyons, 1973), which corresponds to $z_0 \simeq \sqrt{2}$ and a strong diffusion rate $D_{\alpha\alpha}^{\mathrm{SD}}$ given by

$$D_{\alpha\alpha}^{\mathrm{SD}} = \frac{2\ \alpha_{eq,LC}^2}{\tau_B}, \tag{4}$$

such that a flat $J(\alpha_{eq}) = J_{trap}$ can be assumed to infer $J_{omni,eq}$ (i.e., equatorial fluxes are essentially isotropic).

The average omnidirectional equatorial electron fluxes $J_{omni,eq}$ inferred this way from ELFIN measurements at $L \simeq 4.5$ have been compared with the average omnidirectional electron fluxes recorded by the Van Allen Probes (Claudepierre et al., 2021) in 2017–2018, following quiet or disturbed periods. These comparisons demonstrated good agreement from 60 keV to 1.5 MeV, thereby validating the present method (Saint-Girons et al., 2024).

Note that $D_{\alpha\alpha}$ in Equation 1 is proportional to the chorus wave magnetic power B_w^2 at the latitude of cyclotron resonance with electrons (Artemyev et al., 2013; Kennel & Petschek, 1966). Therefore, Equations 1 and 2 can be used to infer the resonant chorus wave power B_w^2 from $J_{prec,eff}/J_{trap}$ measured by ELFIN.

Hereafter, we only keep reliable electron flux data from ELFIN, well above the instrument noise level and with at least 3 consecutive pitch-angle bins with non-null (or non-noisy) fluxes immediately below and above the local loss cone angle. $J_{prec,eff}$ and J_{trap} are calculated over a sliding window of 18-s length, corresponding to 6 full spins of the spacecraft, to obtain more reliable (i.e., less affected by temporary fluctuations) time-averaged precipitating, backscattered, and trapped fluxes. Data such that $J_{prec,eff}/J_{trap}$ at 1 or 2 MeV is higher than $J_{prec,eff}/J_{trap}$ at 390 keV or 520 keV are discarded, to only keep data corresponding to whistler-mode wave-driven electron precipitation (e.g., see Angelopoulos et al., 2023; Tsai et al., 2024). The selected ELFIN measurements represent a data set of ∼2000 pairs ($J_{prec,eff}/J_{trap}$, J_{trap}) for each energy $E \in [60, 140]$ keV to ∼1000 pairs for $E \in [390, 520]$ keV.

3. Statistical Analysis

3.1. Precipitating-To-Trapped Flux Ratio

Figures 1a and 1b show the median (green), 5th percentile (black), and 95th percentile (red) of the precipitating-to-trapped flux ratio $J_{prec,eff}/J_{trap}$ measured by ELFIN in 2020–2022 at $L = 4.5$ and 3–9 MLT, after 3-day periods with $Int(SME) \approx (2-3) \times 10^4$ nT·hr. The results are shown as a function of the inferred equatorial omnidirectional electron flux $J_{omni,eq}$ for 100 and 140 keV electrons, which are the main contributors to the generation of typical chorus waves near $L = 4.5$ (Mourenas et al., 2024). Logarithmic $J_{omni,eq}$ bins of a factor of 1.2 are used, discarding bins containing less than 10 pairs ($J_{prec,eff}/J_{trap}$, $J_{omni,eq}$). The median $J_{prec,eff}/J_{trap}$ remains nearly constant at ≈0.05 − 0.1 over a wide $J_{omni,eq}$ range, but exhibits a rapid increase at high $J_{omni,eq}$, reaching a peak of $J_{prec,eff}/J_{trap} \simeq 0.5$, followed by a similarly rapid decrease and a second lower peak.

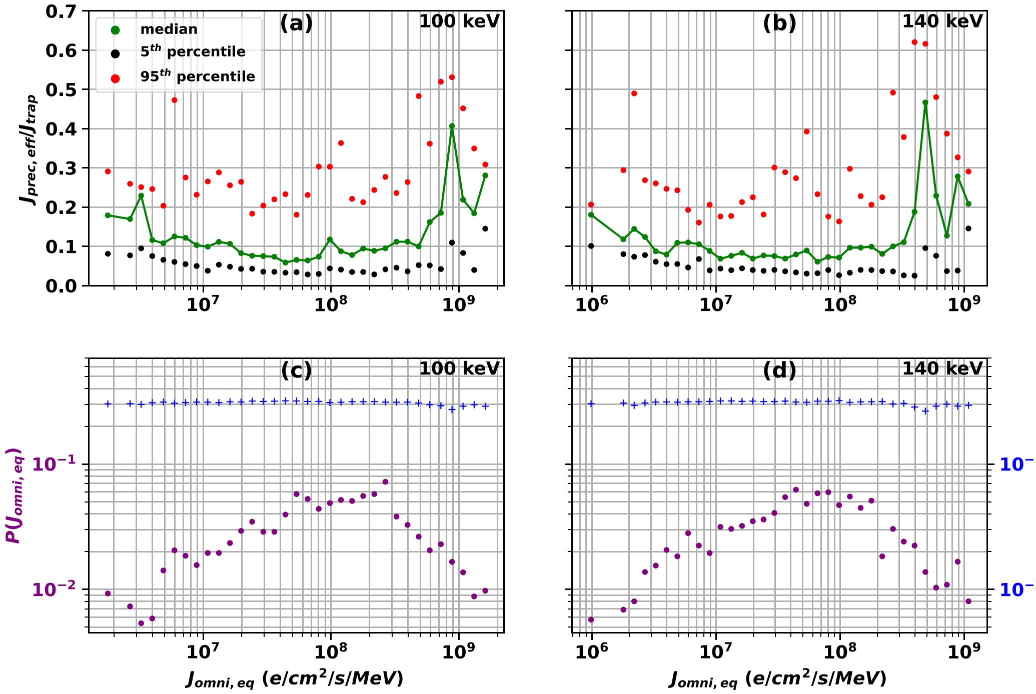

Figure 1. (a), (b) Median (green), 5^{th} percentile (black), and 95^{th} percentile (red), of precipitating-to-trapped electron flux ratio $J_{prec,eff}/J_{trap}$ measured by ELFIN, as a function of equatorial omnidirectional electron flux $J_{omni,eq}$ (in e/cm^2/s/MeV) inferred from ELFIN measurements, at 100 and 140 keV, $L = 4.5$, and 3–9 MLT, following 3-day periods with $Int(SME) \approx (2-3) \times 10^4$ nT·hr. (c), (d) Pitch-angle anisotropy parameter s of the electron distribution (blue) and probability $P(J_{omni,eq})$ of measuring $J_{omni,eq}$ (purple), corresponding to (a), (b).

The anisotropy s of the pitch-angle distribution $J_{omni,eq}(\alpha_{eq}) = \sin^{2s}\alpha_{eq}$ (Summers et al., 2009) is also estimated based on quasi-linear theory (Mourenas et al., 2023, 2024), for equatorial pitch-angles $\alpha_{eq} \in [10°, 90°]$ corresponding to the main population providing free energy for wave growth (Mourenas, Zhang, et al., 2022; Omura et al., 2008; Tao et al., 2017). Figures 1c and 1d show that the pitch-angle anisotropy s (in blue) remains at a level of $s \sim 0.3$ after strong injections, even for the highest $J_{omni,eq}$, in agreement with previous studies (Mauk & Fox, 2010; Mourenas et al., 2024; Olifer et al., 2021; Walton et al., 2023). Another important result in Figures 1c and 1d is that the probability $P(J_{omni,eq})$ of measuring high electron fluxes (purple circles) starts to decrease roughly when $J_{prec,eff}/J_{trap}$ starts to increase toward its peak in Figures 1a and 1b. Such a decrease of $P(J_{omni,eq})$ at high $J_{omni,eq}$ may be the result of a flux limitation mechanism—albeit not a very efficient one, since this decrease is only gradual.

3.2. Chorus Wave Power Gains

The theoretical relativistic linear chorus wave power gain G_{th} was derived by Summers and Shi (2014). Hereafter, we use a fit to their numerical results for an equatorial electron plasma frequency to gyrofrequency ratio $\Omega_{pe}/\Omega_{ce} \approx 4.5$, a typical value at $L \approx 4.5$ during disturbed periods (Agapitov et al., 2019). This gives $G_{th} \approx \Xi\, J_{omni,eq}\, s^B L^4 E$, with Ξ a constant and $B = \max\left((0.4/E[\mathrm{MeV}])^{2/5}, 1\right)$, for $0.1-0.8$ MeV and $s \approx 0.25-0.5$ (Mourenas et al., 2024).

The mean and median (red and green circles, respectively) of $(J_{prec,eff}/J_{trap})^2$ are displayed in Figures 2a and 2b as a function of the normalized theoretical linear wave power gain, $G_{th}/(\Xi\, L^4 E) = J_{omni,eq}\, s^B$ for fixed $L = 4.5$ and fixed $E = 100$ keV or 140 keV, using the same data as in Figure 1. Least squares linear fits to 6 consecutive points of the logarithm of $(J_{prec,eff}/J_{trap})^2$, at its peak and immediately before its peak, are shown by solid lines for the mean (red) and median (green). These fitted increases of the mean and median of $(J_{prec,eff}/J_{trap})^2$ exceed the global mean and median (shown by horizontal dashed lines), suggesting their statistical significance. The high

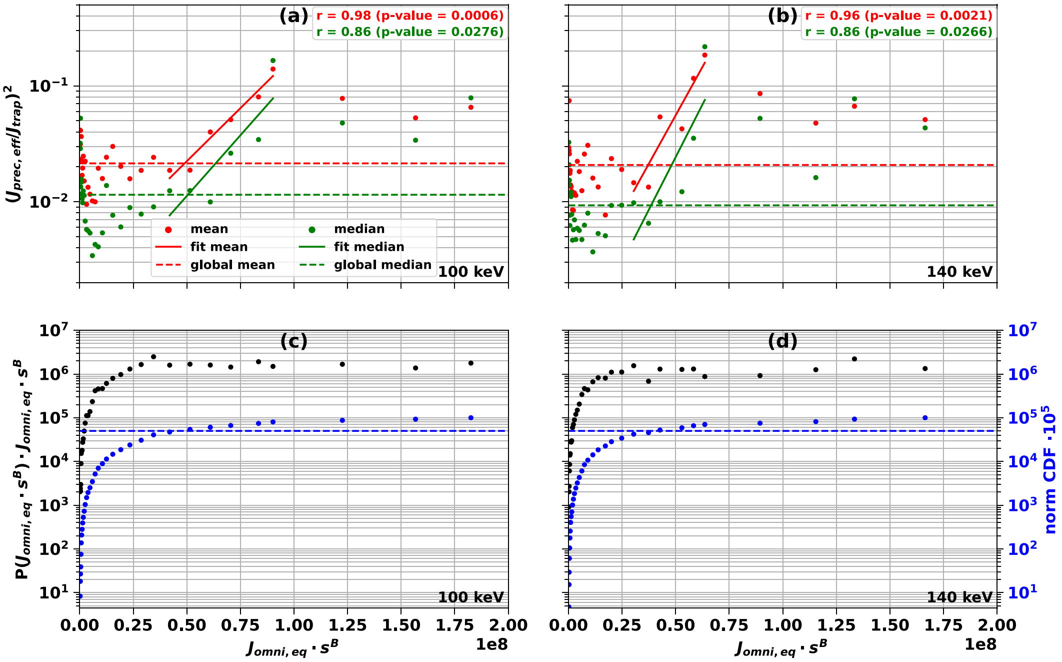

Figure 2. (a), (b) Mean and median $(J_{prec,eff}/J_{trap})^2$ measured by ELFIN (red and green circles, respectively), as a function of $J_{omni,eq}\ s^B$ (with $J_{omni,eq}$ in e/cm^2/s/MeV) inferred from ELFIN measurements, at 100 and 140 keV, $L = 4.5$, and 3–9 MLT, following 3-day periods with $Int(SME) = (2-3)\times 10^4$ nT·hr. Solid lines show least squares fits (their Pearson r and its $p - value$ are noted). (c), (d) Corresponding inferred time-weighted normalized theoretical linear wave power gain, $P(J_{omni,eq}\ s^B)\times(J_{omni,eq}\ s^B)$ (black circles), and its Cumulative Distribution Function (CDF) (blue circles), with the CDF= 0.5 level marked by a dashed blue line (all CDF values are multiplied by 10^5).

Pearson correlation coefficients, $r \simeq 0.86 - 0.98$, along with low p-values (ranging from 0.0006 to 0.0276) from the Student t-test (Press et al., 1992), confirm a statistically significant linear relationship between the logarithm of $(J_{prec,eff}/J_{trap})^2$ and $J_{omni,eq}\ s^B$. This relationship holds at a confidence level greater than 97% for all fits and exceeding 99.8% for the two best fits to the mean. Since most fitted points are such that $(J_{prec,eff}/J_{trap})^2 > 0.01$, the fitted $(J_{prec,eff}/J_{trap})^2$ is approximately proportional to the pitch-angle diffusion rate toward the loss cone, $D_{\alpha\alpha}$, at fixed L and E (Mourenas et al., 2024).

The Cumulative Distribution Function (CDF) of the inferred time-weighted normalized theoretical wave power gain, $P(J_{omni,eq}\ s^B)\times(J_{omni,eq}\ s^B)$ (multiplied by 10^5 for display purposes, with P the normalized probability), is displayed (blue circles) in Figures 2c and 2d. The best fits in Figures 2a and 2b start when CDF ≈ 0.5 in Figures 2c and 2d. Therefore, half of the total time-weighted theoretical linear wave power gain is at lower $J_{omni,eq}\ s^B$ than the fits. This lower part of the G_{th} distribution corresponds to the most frequent electron fluxes, which maintain a significant average wave power at $L \sim 4.5$, through their presence with different levels at various L-shells and the spreading of the generated waves to nearby L-shells (Chen et al., 2013). The nearly constant and relatively high $J_{prec,eff}/J_{trap}$ level at low $J_{omni,eq}\ s^B$ in Figure 2 is consistent with the presence of such a significant background average wave power at all times following 3-day periods with $Int(SME) = (2-3)\times 10^4$ nT·hr.

Figures 2c and 2d show that the inferred time-weighted normalized theoretical wave power gain, $P(J_{omni,eq}\ s^B)\times(J_{omni,eq}\ s^B)$ (black circles), rapidly increases as $J_{omni,eq}\ s^B$ increases, before saturating at a nearly constant level. This saturation corresponds to a decrease of the probability $P(J_{omni,eq}\ s^B)$ of measuring a high $J_{omni,eq}\ s^B$, approximately like $1/(J_{omni,eq}\ s^B)$. The strong increase of $(J_{prec,eff}/J_{trap})^2$ in Figures 2a and 2b coincides with this saturation of $P(J_{omni,eq}\ s^B)\times(J_{omni,eq}\ s^B)$ in Figures 2c and 2d. This suggests that the trapped electron flux may be limited by increased wave-driven electron loss into the atmosphere.

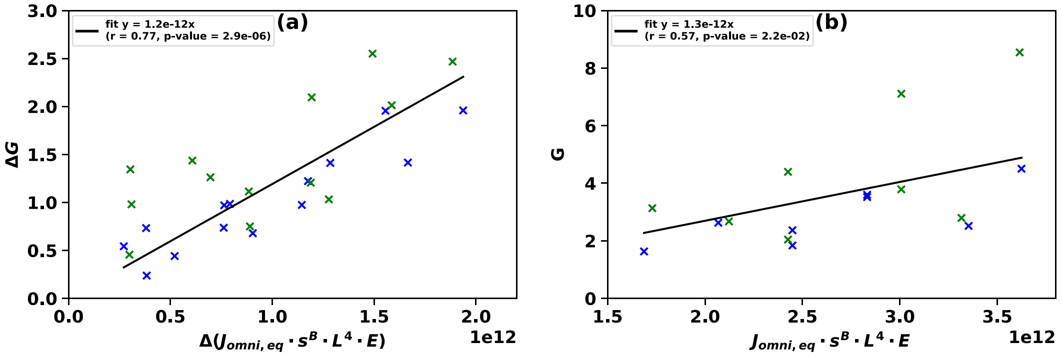

Figure 3. (a) Wave power gain variation, ΔG, inferred, using Equation 5, from the variation of $\langle (J_{prec,eff}/J_{trap})^2 \rangle$ between two $J_{omni,eq}\ s^B L^4 E$ values separated by $\Delta(J_{omni,eq}\ s^B L^4 E)$ (with $J_{omni,eq}$ in e/cm^2/s/MeV and E in keV), for 100 keV (blue) and 140 keV (green) at $L = 4.5$ and 3–9 MLT, following 3-day periods with $Int(SME) = (2 - 3) \times 10^4$ nT·hr. We use six-point series of $\langle (J_{prec,eff}/J_{trap})^2 \rangle$ fitted in Figure 2. A black line shows a least squares linear fit (its formula, the Pearson correlation coefficient r and its $p - value$, are provided in the panel). (b) Same as (a) for wave power gains G inferred, using Equation 6, from the measured $\langle (J_{prec,eff}/J_{trap})^2 \rangle$ values.

While these findings could be linked to the Kennel-Petschek limit, it is worth noting that the Kennel-Petschek mechanism should a priori result in a more abrupt upper limit on $J_{omni,eq}$ than what we observe in Figures 1 and 2. The Kennel-Petschek mechanism indeed anticipates an exponential increase in both wave power and wave-driven electron loss when $J_{omni,eq}$ exceeds the presumed flux limit, $J^{KP}_{omni,eq}$ (Kennel & Petschek, 1966; Summers & Shi, 2014). The observed gradual saturation of $J_{omni,eq}$ could therefore be due to a more dynamical flux limitation mechanism, corresponding to an increase of $J_{omni,eq}$ until the total numbers of injected and precipitated electrons per second balance each other (Etcheto et al., 1973; Mourenas et al., 2023).

To check this conjecture, we estimate the variation of the actual wave power gain G as a function of $J_{omni,eq}$ and G_{th}. G can be inferred from ELFIN measurements, using a method proposed by Mourenas et al. (2024) based on quasi-linear diffusion theory (Kennel & Petschek, 1966). We assume that Ω_{pe}/Ω_{ce} and the wave frequency to gyrofrequency ratio, ω/Ω_{ce}, remain approximately constant at $L = 4.5$ and 3–9 MLT during periods of similar geomagnetic activity, as in statistical observations (Agapitov et al., 2018, 2019). The variation of the actual wave power gain G between two values of $G_{th} = J_{omni,eq}\ s^B L^4 E$ can then be expressed as

$$\Delta G = G_2 - G_1 = \ln\left(\frac{D_{\alpha\alpha,2}}{D_{\alpha\alpha,1}}\right) = \ln\left(\left(\frac{z_{0,1}}{z_{0,2}}\right)^2\right), \tag{5}$$

with $D_{\alpha\alpha}$ the wave-driven pitch-angle diffusion rate near the loss-cone, which is proportional to the chorus wave power B_w^2 at the latitude of cyclotron resonance with electrons (Mourenas et al., 2024). Equation 5, with the help of Equation 2, directly provides ΔG as a function of two values of the measured $J_{prec,eff}/J_{trap}$ corresponding to two different values of $G_{th} = \Xi\ J_{omni,eq}\ s^B L^4 E$ (Mourenas et al., 2024).

To derive the actual wave power gain G, we further assume that it is roughly proportional to the theoretical linear wave power gain G_{th}, as in the derivation of the Kennel-Petschek flux limit (Kennel & Petschek, 1966; Summers & Shi, 2014). This gives $G_2/G_1 \approx G_{th,2}/G_{th,1}$, allowing us to express $G = G_1$ in terms of ΔG as (Mourenas et al., 2024):

$$G = G_1 \approx \Delta G \cdot \left(\frac{G_{th,2}}{G_{th,1}} - 1\right)^{-1}. \tag{6}$$

Figure 3a shows wave power gain variations ΔG, inferred from the variation of $\langle (J_{prec,eff}/J_{trap})^2 \rangle$ between two different $J_{omni,eq}\ s^B L^4 E$ values, as a function of their difference $\Delta(J_{omni,eq}\ s^B L^4 E)$, for 100 and 140 keV electrons at $L = 4.5$ and 3–9 MLT, following 3-day periods with $Int(SME) = (2 - 3) \times 10^4$ nT·hr. We use the six-point series of $\langle (J_{prec,eff}/J_{trap})^2 \rangle$ values which have been fitted in Figure 2. Figure 3b shows the actual wave power gains G inferred from the same six-point series. In this case, we only use pairs of points separated by a third point in the abscissa, preventing the term $(G_{th,2}/G_{th,1} - 1)^{-1}$ in Equation 6 from taking on arbitrarily large values, which would yield less reliable estimates (Mourenas et al., 2024).

The high Pearson correlation coefficients, $r = 0.77$ and $r = 0.57$, of the least squares linear fits in Figures 3a and 3b, and the low p-values of $\simeq 2.9 \times 10^{-6}$ and 2.2×10^{-2} from the Student t-test, indicate a statistically significant linear relationship between the actual gain G and the normalized theoretical linear gain G_{th}/Ξ. The corresponding confidence levels are 99.999% and 97.8%, respectively. The two best fits in Figure 3 give $G \simeq 1.25 \times 10^{-12} \times J_{omni,eq}\, s^B L^4 E$, with $J_{omni,eq}$ in e/cm^2/s/MeV and E in keV. This linear relationship between G and G_{th} implies an exponential increase of the wave power B_w^2 as $J_{omni,eq}\, s^B L^4 E$ increases from $\sim 1.5 \times 10^{12}$ up to at least 3.6×10^{12}. Actual gains reach values of $G \approx 4.5 - 8.5$ at high $J_{omni,eq}$, consistent with results from a previous case study (Mourenas et al., 2024).

3.3. Saturation of Electron Flux and Resonant Chorus Wave Power

We now examine the saturation of equatorial electron fluxes, observed in Figures 1 and 2. Figure 4a presents the probability $P\left(J_{omni,eq}\, s^B L^4 E\right)$ of measuring electron fluxes $J_{omni,eq}$ that correspond to a normalized theoretical linear wave power gain $G_{th}/\Xi = J_{omni,eq}\, s^B L^4 E$. $P\left(J_{omni,eq}\, s^B L^4 E\right)$ is shown as a function of $J_{omni,eq}\, s^B L^4 E$ for energies from 60 to 520 keV at $L = 4.5$ and 3–9 MLT, following 3-day periods with $Int(SME) = (2 - 3) \times 10^4$ nT·hr in 2020–2022. Initially, $P\left(J_{omni,eq}\, s^B L^4 E\right)$ slowly increases as $J_{omni,eq}\, s^B L^4 E$ rises. However, it then steeply decreases by a factor of ~ 5, following a trend resembling $\sim 1/\left(J_{omni,eq}\, s^B L^4 E\right)^{1.1}$, as $J_{omni,eq}\, s^B L^4 E$ increases from 1.6×10^{12} to 7×10^{12}. This indicates a progressive saturation of $60 - 520$ keV electron fluxes above a threshold $J_{omni,eq}\, s^B L^4 E \approx 1.6 \times 10^{12}$. $P\left(J_{omni,eq}\, s^B L^4 E\right)$ reaches its lowest value at $J_{omni,eq}\, s^B L^4 E \approx 8 \times 10^{12}$ and remains at this level up to $J_{omni,eq}\, s^B L^4 E \approx 5 \times 10^{13}$.

Figure 4b displays the average and median magnetic amplitudes B_w (circles and crosses, respectively) of the chorus waves that precipitate 100 keV (blue) and 140 keV (green) electrons, inferred from the mean or median of $(J_{prec,eff}/J_{trap})^2$ measured by ELFIN. We assume that electron scattering into the loss cone occurs via cyclotron resonance at magnetic latitudes $\lambda_R[^\circ] = 80 \cdot (0.35 - \omega/\Omega_{ce})$, where parallel chorus waves of average wave-power-weighted frequency ω/Ω_{ce} are predominantly observed in Van Allen Probes statistics (Agapitov et al., 2018). By combining this empirical formula for λ_R with the cyclotron resonance condition, we find $\lambda_R \sim 13^\circ - 16^\circ$ and $\omega/\Omega_{ce} \sim 0.18 - 0.15$ for $100 - 140$ keV electrons (assuming $\Omega_{pe}/\Omega_{ce} = 4.5$ at $L = 4.5$). Substituting these parameters in $D_{\alpha\alpha} = A \times B_w^2$ (Albert, 2005; Artemyev et al., 2013; Glauert & Horne, 2005) provides the coefficient A. Using Equations 1 and 2, we can finally express B_w as a function of $J_{prec,eff}/J_{trap}$. The inferred B_w depends only weakly on Ω_{pe}/Ω_{ce} and ω/Ω_{ce} (Artemyev et al., 2013).

The global mean and median inferred amplitudes, $B_w \approx 35 - 65$ pT, are consistent with statistical time-averaged chorus wave amplitudes measured by the Van Allen Probes at latitudes $\lambda = 13^\circ - 16^\circ$ and 4–12 MLT during disturbed periods with $Kp \approx 4 - 5$ (Agapitov et al., 2018). In Figure 4b, the inferred average wave amplitude remains nearly constant at $B_w \approx 65$ pT up to $J_{omni,eq}\, s^B L^4 E \approx 2 \times 10^{12}$. Above this threshold, the average B_w steeply increases, reaching $B_w \approx 250$ pT at $J_{omni,eq}\, s^B L^4 E \approx 3.6 \times 10^{12}$. This behavior aligns with the exponential increase $B_w[\text{pT}] = 55 \times \exp\left(6.25 \times 10^{-13}\left(J_{omni,eq}\, s^B L^4 E - 1.8 \times 10^{12}\right)\right)$ (red curve) derived from the best fits in Figure 3. This exponential increase of B_w with the theoretical linear gain $G_{th} = \Xi\, J_{omni,eq}\, s^B L^4 E$, coupled with the concurrent decline in the probability $P\left(J_{omni,eq}\, s^B L^4 E\right)$ of observing such high fluxes in Figure 4a, is consistent with the Kennel-Petschek model.

The minimum of $P\left(J_{omni,eq}\, s^B L^4 E\right)$ is observed in Figure 4a at $J_{omni,eq}\, s^B L^4 E \approx 8 \times 10^{12}$. This nearly coincides with the point in Figure 4b where the fitted B_w (red curve) reaches the strong diffusion level (shown by blue or green dashed lines), corresponding to the shortest electron lifetime, $\min(\tau_L) = 1/D_{\alpha\alpha}^{\text{SD}} \approx 50 - 70$ s at $100 - 140$ keV (Kennel, 1969; Lyons, 1973). However, when $J_{omni,eq}\, s^B L^4 E$ increases above 4×10^{12}, the actual average B_w does not attain the strong diffusion level. Instead, it gradually decreases from 150 to 80 pT at

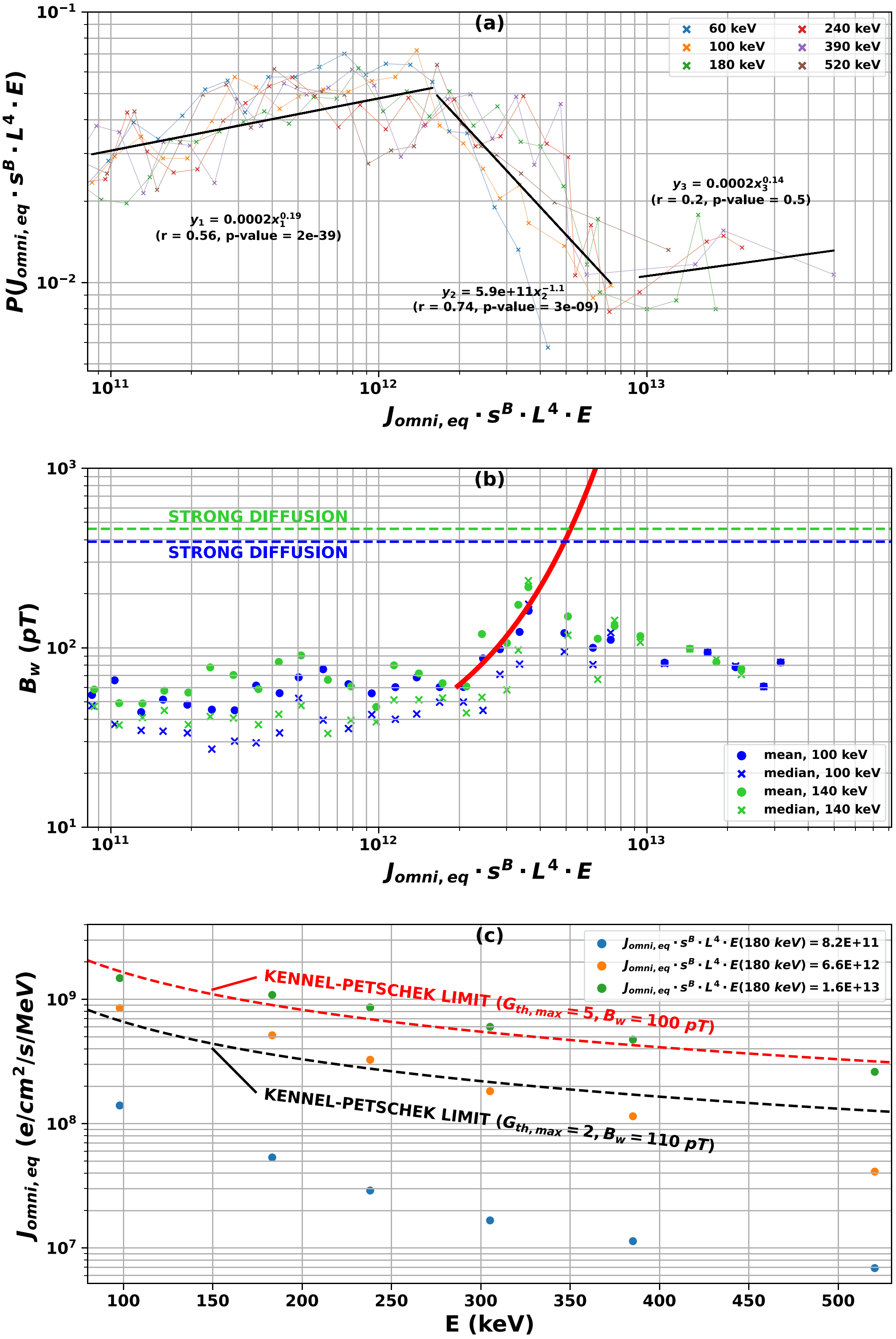
(a)
60 keV
100 keV
180 keV
240 keV
390 keV
520 keV
$y_1 = 0.0002x_1^{0.19}$
(r = 0.56, p-value = 2e-39)
$y_2 = 5.9e{+}11x_2^{-1.1}$
(r = 0.74, p-value = 3e-09)
$y_3 = 0.0002x_3^{0.14}$
(r = 0.2, p-value = 0.5)
$P(J_{omni,eq} \cdot s^B \cdot L^4 \cdot E)$
10^{-1}
10^{-2}
10^{11}
10^{12}
10^{13}
$J_{omni,eq} \cdot s^B \cdot L^4 \cdot E$
(b)
STRONG DIFFUSION
STRONG DIFFUSION
mean, 100 keV
median, 100 keV
mean, 140 keV
median, 140 keV
B_w (pT)
10^3
10^2
10^1
10^{11}
10^{12}
10^{13}
$J_{omni,eq} \cdot s^B \cdot L^4 \cdot E$
(c)
$J_{omni,eq} \cdot s^B \cdot L^4 \cdot E(180\ keV) = 8.2E{+}11$
$J_{omni,eq} \cdot s^B \cdot L^4 \cdot E(180\ keV) = 6.6E{+}12$
$J_{omni,eq} \cdot s^B \cdot L^4 \cdot E(180\ keV) = 1.6E{+}13$
KENNEL-PETSCHEK LIMIT ($G_{th,max} = 5, B_w = 100$ pT)
KENNEL-PETSCHEK LIMIT ($G_{th,max} = 2, B_w = 110$ pT)
$J_{omni,eq}$ (e/cm^2/s/MeV)
10^9
10^8
10^7
100
150
200
250
300
350
400
450
500
E (keV)

Figure 4.

$J_{omni,eq}\ s^B L^4 E = 2.5 \times 10^{13}$. Meanwhile, the probability $P(J_{omni,eq}\ s^B L^4 E)$ of measuring such high fluxes remains relatively low and stable in Figure 4a.

The observed saturation of the average B_w when $G_{th}/\Xi = J_{omni,eq}\ s^B L^4 E > 4 \times 10^{12}$ implies that electron losses cannot increase faster than $J_{omni,eq}$ anymore. As a result, $J_{omni,eq}$ can exceed any predetermined upper limit, such as the Kennel-Petschek limit, during sufficiently strong electron injections (Etcheto et al., 1973; Mourenas et al., 2023; Schulz, 1974). This is consistent with the existence of a second, more dynamical upper limit, $J^{up}_{omni,eq}(E)$, which represents an attractor for the system dynamics in the presence of both chorus wave-driven pitch-angle and energy diffusion, regardless of the wave amplitude B_w (Hua, Bortnik, & Ma, 2022; Mourenas et al., 2023). In this case, $J_{omni,eq}$ may continue to increase as long as $J_{omni,eq}(E)$ decreases more steeply toward higher energy than the steady-state attractor shape $J^{up}_{omni,eq}(E) \approx 1/E$, and the total number of precipitated $0.1 - 1$ MeV electrons per second does not yet balance the total number of injected electrons per second (Mourenas et al., 2023). This could explain the finite residual probability of observing very high trapped fluxes in Figure 4a.

The observed saturation of the average B_w may be ascribed to various physical processes. First, the time-averaged B_w is expected to remain sensibly below the strong diffusion level, because strong diffusion would otherwise flatten the pitch-angle distribution ($s \to 0$), suppressing the growth of resonant waves at $\omega/\Omega_{ce} > s/(1+s)$ (Summers & Shi, 2014). Second, nonlinear chorus wave growth should lead to a saturation of B_w near an optimum amplitude $B_{w,opt}$ proportional to $J_{omni,eq}$ (Omura & Nunn, 2011), potentially limiting the average B_w. Third, when chorus waves are simultaneously generated at different frequencies (Katoh & Omura, 2016), resonance overlap should occur at sufficiently high B_w, leading to a stochastization of particle trajectories and quenching nonlinear wave growth (Mourenas, Zhang, et al., 2022). Fourth, Landau damping may limit the mid-latitude B_w at 3–9 MLT during the strongest injections (Chen et al., 2013).

Figure 4c shows the average fluxes $J_{omni,eq}(E)$ inferred from ELFIN measurements for three selected normalized theoretical gains $G_{th}/\Xi = J_{omni,eq}\ s^B L^4 E \simeq 8.2 \times 10^{11}$ (blue circles), 6.6×10^{12} (orange circles), and 1.6×10^{13} (green circles) in Figure 4a. Each $J_{omni,eq}(E)$ profile is averaged over roughly 100 individual measurements at each E. For a low theoretical linear gain, $J_{omni,eq}\ s^B L^4 E \simeq 8 \times 10^{11}$, $J_{omni,eq}(E)$ is low and steeply decreases with increasing energy (blue circles). For $J_{omni,eq}\ s^B L^4 E = 6.6 \times 10^{12}$, that is, above the flux saturation threshold, $J_{omni,eq}(E)$ is much higher and decreases less steeply at higher energies (orange circles). At $100 - 300$ keV, $J_{omni,eq}$ now reaches the Kennel-Petschek limit $J^{KP}_{omni,eq}$ (black dashed line) corresponding to a theoretical linear gain $G_{th} = \Xi\ J_{omni,eq}\ s^B L^4 E = 2$ for $L = 4.5$, $\Omega_{pe}/\Omega_{ce} \simeq 4.5$, and $s \simeq 0.3$ (Summers & Shi, 2014). However, $J_{omni,eq}$ still remains much lower than this limit at $390 - 520$ keV. Finally, for a very high $J_{omni,eq}\ s^B L^4 E = 1.6 \times 10^{13}$, $J_{omni,eq}$ (green circles) reaches the Kennel-Petschek limit $J^{KP}_{omni,eq}$ corresponding to a linear gain $G_{th} = 5$ (red dashed line) from 100 to 520 keV, with a scaling $J_{omni,eq}(E) \sim J^{KP}_{omni,eq}(E) \sim 1/E$ (Summers & Shi, 2014).

The results in Figure 4 provide clear statistical evidence of a saturation of the equatorial electron flux $J_{omni,eq}$ at $L \simeq 4.5$ after prolonged disturbed periods. However, they also demonstrate that $J_{omni,eq}$ can significantly exceed the traditional Kennel-Petschek limit $J^{KP}_{omni,eq}$ for $G_{th,\max} = 3$. A few recent works have similarly shown that equatorial $30 - 100$ keV electron fluxes can sometimes exceed this limit (Chakraborty et al., 2022; Olifer et al., 2023; Walton et al., 2023). But Figure 4 additionally provides a potential explanation, based on the resonant chorus wave power simultaneously inferred from ELFIN measurements. Indeed, the average amplitude of the resonant chorus waves precipitating these electrons remains the same ($B_w \simeq 100$ pT) between $J_{omni,eq}\ s^B L^4 E = 6.6 \times 10^{12}$ and $J_{omni,eq}\ s^B L^4 E = 1.6 \times 10^{13}$ in Figure 4b, when the linear gain G_{th}

Figure 4. (a) Probability $P(J_{omni,eq}\ s^B L^4 E)$ of measuring electron fluxes $J_{omni,eq}$ corresponding to a normalized theoretical linear wave power gain $J_{omni,eq}\ s^B L^4 E$ (with $J_{omni,eq}$ in e/cm^2/s/MeV and E in keV), as a function of $J_{omni,eq}\ s^B L^4 E$, for 60–520 keV (colored crosses) at $L = 4.5$ and 3–9 MLT after prolonged disturbed periods, inferred from ELFIN 2020–2022 measurements, with least squares fits (black lines). (b) Average amplitude B_w (in pT) of chorus waves precipitating these electrons into the atmosphere, inferred from mean or median (circles and crosses, respectively) measured $(J_{prec,eff}/J_{trap})^2$, for 100 keV (blue) and 140 keV (green). A red curve shows the exponential increase deduced from Figure 3. Dashed lines show the strong diffusion limit. (c) Average $J_{omni,eq}(E)$ inferred from ELFIN measurements, for three values of $J_{omni,eq}\ s^B L^4 E$ in (a). The Kennel-Petschek limit $J^{KP}_{omni,eq}(E)$ for $\Omega_{pe}/\Omega_{ce} \approx 4.5$ and $s \simeq 0.3$ is shown for $G_{th,\max} = 2$ and $G_{th,\max} = 5$ (black and red dashed lines), corresponding to $B_w \simeq 110$ pT and $B_w \simeq 100$ pT in panel (b), respectively.

simultaneously increases from 2 to 5. In such a case, the Kennel-Petschek mechanism should become less effective, consistent with the soft flux limitation observed in Figure 4a.

4. Conclusions

Various works suggest that $0.1 - 0.5$ MeV electron fluxes are capped at the Kennel-Petschek limit in the outer radiation belt (Olifer et al., 2021, 2022; Summers et al., 2009). In the present study, we used low-altitude pitch-angle resolved ELFIN measurements of $60 - 520$ keV electron fluxes, following strong substorm-related injections, to infer both equatorial omnidirectional electron fluxes and wave-driven electron pitch-angle diffusion rates near the loss cone. This enabled for the first time a fine simultaneous analysis of equatorial electron fluxes and of the amplitude of the middle-latitude cyclotron-resonant chorus waves directly responsible for the precipitation of these electrons, providing novel information on the flux limitation process. We notably demonstrated that the main drop of the probability of measuring high fluxes coincides with an exponential increase of the resonant chorus wave power, at a rate proportional to the theoretical linear wave power gain. This represents the first statistical corroboration of two key elements of the Kennel-Petschek model (Kennel & Petschek, 1966; Summers & Shi, 2014).

But we also found that when the theoretical linear wave power gain increases from 2 to 5, both the probability of measuring high fluxes and the inferred average amplitude of the resonant chorus waves precipitating these electrons remain nearly constant. This unexpected saturation of chorus wave amplitudes corresponds to a softer flux limit than in the traditional Kennel-Petschek model. It may lead to another, more dynamical upper limit, which represents an attractor for a system with both wave-driven pitch-angle and energy diffusion, regardless of the wave amplitude (Hua, Bortnik, & Ma, 2022; Mourenas et al., 2023). This might allow for extreme fluxes during extreme events (Etcheto et al., 1973; Mourenas et al., 2023). Future research should explore nonlinear effects (Mourenas et al., 2018; Mourenas, Zhang, et al., 2022; Summers et al., 2012) and strong diffusion (Kasahara et al., 2019) to improve our understanding of flux saturation mechanisms.

Data Availability Statement

ELFIN data is freely available at https://data.elfin.ucla.edu/. The *SME* index (Gjerloev, 2012) is available at the SuperMAG data archive at https://supermag.jhuapl.edu/indices/. Data access and processing was done using SPEDAS V3.1 (Angelopoulos et al., 2019).

Acknowledgments
A.V.A., X.J.Z., and V.A. acknowledge NASA awards 80NSSC20K1270, 80NSSC23K0403, 80NSSC24K0558, 80NSSC23K1038, and NSF grant AGS-2329897. We are grateful to NASA's CubeSat Launch Initiative for ELFIN's successful launch. We acknowledge early support of ELFIN project by the AFOSR under its University Nanosat Program; by the UNP-8 project, contract FA9453-12-D-0285; and by the California Space Grant program. We acknowledge critical contributions of numerous volunteer ELFIN team student members.

References

Agapitov, O. V., Mourenas, D., Artemyev, A. V., Hospodarsky, G., & Bonnell, J. W. (2019). Time scales for electron quasi-linear diffusion by lower-band chorus waves: The effects of ω_{pe}/Ω_{ce} dependence on geomagnetic activity. *Geophysical Research Letters*, *46*(12), 6178–6187. https://doi.org/10.1029/2019GL083446

Agapitov, O. V., Mourenas, D., Artemyev, A. V., Mozer, F. S., Hospodarsky, G., Bonnell, J., & Krasnoselskikh, V. (2018). Synthetic empirical chorus wave model from combined van allen Probes and cluster statistics. *Journal of Geophysical Research (Space Physics)*, *123*(1), 297–314. https://doi.org/10.1002/2017JA024843

Albert, J. M. (2005). Evaluation of quasi-linear diffusion coefficients for whistler mode waves in a plasma with arbitrary density ratio. *J. Geophys. Res. (Space Physics)*, *110*(A3), 3218. https://doi.org/10.1029/2004JA010844

Angelopoulos, V., Cruce, P., Drozdov, A., Grimes, E. W., Hatzigeorgiu, N., King, D. A., et al. (2019). The space physics environment data analysis system (SPEDAS). *Space Science Reviews*, *215*(1), 9. https://doi.org/10.1007/s11214-018-0576-4

Angelopoulos, V., Tsai, E., Bingley, L., Shaffer, C., Turner, D. L., Runov, A., et al. (2020). The ELFIN mission. *Space Science Reviews*, *216*(5), 103. https://doi.org/10.1007/s11214-020-00721-7

Angelopoulos, V., Zhang, X. J., Artemyev, A. V., Mourenas, D., Tsai, E., Wilkins, C., et al. (2023). Energetic electron precipitation driven by electromagnetic ion cyclotron waves from ELFIN's low altitude perspective. *Space Science Reviews*, *219*(5), 37. https://doi.org/10.1007/s11214-023-00984-w

Artemyev, A. V., Mourenas, D., Agapitov, O. V., & Krasnoselskikh, V. V. (2013). Parametric validations of analytical lifetime estimates for radiation belt electron diffusion by whistler waves. *Annales Geophysicae*, *31*(4), 599–624. https://doi.org/10.5194/angeo-31-599-2013

Artemyev, A. V., Mourenas, D., Zhang, X. J., & Vainchtein, D. (2022). On the incorporation of nonlinear resonant wave-particle interactions into radiation belt models. *Journal of Geophysical Research (Space Physics)*, *127*(9), e30853. https://doi.org/10.1029/2022JA030853

Artemyev, A. V., Neishtadt, A. I., Vasiliev, A. A., & Mourenas, D. (2021). On a transitional regime of electron resonant interaction with whistler-mode waves in inhomogeneous space plasma. *Physical Review*, *104*(5), 055203. https://doi.org/10.1103/PhysRevE.104.055203

Carlson, C. R., Helliwell, R. A., & Carpenter, D. L. (1985). Variable frequency VLF signals in the magnetosphere: Associated phenomena and plasma diagnostics. *J. Geophys. Res. (Space Physics)*, *90*(A2), 1507–1521. https://doi.org/10.1029/JA090iA02p01507

Chakraborty, S., Mann, I. R., Watt, C. E. J., Rae, I. J., Olifer, L., Ozeke, L. G., et al. (2022). Intense chorus waves are the cause of flux-limiting in the heart of the outer radiation belt. *Scientific Reports*, *12*(1), 21717. https://doi.org/10.1038/s41598-022-26189-9

Chen, L., Thorne, R. M., Li, W., & Bortnik, J. (2013). Modeling the wave normal distribution of chorus waves. *J. Geophys. Res. (Space Physics)*, *118*(3), 1074–1088. https://doi.org/10.1029/2012JA018343

Claudepierre, S. G., Blake, J. B., Boyd, A. J., Clemmons, J. H., Fennell, J. F., Gabrielse, C., et al. (2021). The magnetic electron ion spectrometer: A review of on-orbit sensor performance, data, operations, and science. *Space Science Reviews*, *217*(8), 80. https://doi.org/10.1007/s11214-021-00855-2

Etcheto, J., Gendrin, R., Solomon, J., & Roux, A. (1973). A self-consistent theory of plasmaspheric hiss. *Journal of Geophysical Research*, *78*(34), 8150–8166. https://doi.org/10.1029/JA078i034p08150

Fu, X., Cowee, M. M., Friedel, R. H., Funsten, H. O., Gary, S. P., Hospodarsky, G. B., et al. (2014). Whistler anisotropy instabilities as the source of banded chorus: Van Allen Probes observations and particle-in-cell simulations. *Journal of Geophysical Research (Space Physics)*, *119*(10), 8288–8298. https://doi.org/10.1002/2014JA020364

Gjerloev, J. W. (2012). The SuperMAG data processing technique. *J. Geophys. Res. (Space Physics)*, *117*(A9), A09213. https://doi.org/10.1029/2012JA017683

Glauert, S. A., & Horne, R. B. (2005). Calculation of pitch angle and energy diffusion coefficients with the PADIE code. *Journal of Geophysical Research*, *110*(A4), 4206. https://doi.org/10.1029/2004JA010851

Horne, R. B., Thorne, R. M., Glauert, S. A., Albert, J. M., Meredith, N. P., & Anderson, R. R. (2005). Timescale for radiation belt electron acceleration by whistler mode chorus waves. *J. Geophys. Res. (Space Physics)*, *110*(A3), 3225. https://doi.org/10.1029/2004JA010811

Hua, M., & Bortnik, J. (2024). Upper limit of outer belt electron acceleration and their controlling geomagnetic conditions: A comparison of storm and non-storm events. *Geophysical Research Letters*, *51*(13), e2024GL109612. https://doi.org/10.1029/2024GL109612

Hua, M., Bortnik, J., Chu, X., Aryan, H., & Ma, Q. (2022). Unraveling the critical geomagnetic conditions controlling the upper limit of electron fluxes in the Earth's outer radiation belt. *Geophysical Research Letters*, *49*(22), e2022GL101096. https://doi.org/10.1029/2022GL101096

Hua, M., Bortnik, J., & Ma, Q. (2022). Upper limit of outer radiation belt electron acceleration driven by whistler-mode chorus waves. *Geophysical Research Letters*, *49*(15), e2022GL099618. https://doi.org/10.1029/2022GL099618

Kasahara, S., Miyoshi, Y., Kurita, S., Yokota, S., Keika, K., Hori, T., et al. (2019). Strong diffusion of energetic electrons by equatorial chorus waves in the midnight-to-dawn sector. *Geophysical Research Letters*, *46*(22), 12685–12692. https://doi.org/10.1029/2019GL085499

Katoh, Y., & Omura, Y. (2016). Electron hybrid code simulation of whistler-mode chorus generation with real parameters in the Earth's inner magnetosphere. *Earth Planets and Space*, *68*(1), 192. https://doi.org/10.1186/s40623-016-0568-0

Kennel, C. F. (1969). Consequences of a magnetospheric plasma. *Reviews of Geophysics and Space Physics*, *7*(1–2), 379–419. https://doi.org/10.1029/RG007i001p00379

Kennel, C. F., & Petschek, H. E. (1966). Limit on stably trapped particle fluxes. *J. Geophys. Res. (Space Physics)*, *71*, 1–28. https://doi.org/10.1029/jz071i001p00001

Lyons, L. R. (1973). Comments on pitch angle diffusion in the radiation belts. *J. Geophys. Res. (Space Physics)*, *78*(28), 6793–6797. https://doi.org/10.1029/JA078i028p06793

Marshall, R. A., & Bortnik, J. (2018). Pitch angle dependence of energetic electron precipitation: Energy deposition, backscatter, and the bounce loss cone. *J. Geophys. Res. (Space Physics)*, *123*(3), 2412–2423. https://doi.org/10.1002/2017JA024873

Mauk, B. H., & Fox, N. J. (2010). Electron radiation belts of the solar system. *J. Geophys. Res. (Space Physics)*, *115*(A12), 12220. https://doi.org/10.1029/2010JA015660

Meredith, N. P., Horne, R. B., Shen, X.-C., Li, W., & Bortnik, J. (2020). Global model of whistler mode chorus in the near-equatorial region (\vert {\lambda}_{m}\vert \lt 18\textdegree). *Geophysical Research Letters*, *47*(11), e2020GL087311. https://doi.org/10.1029/2020GL087311

Mourenas, D., Agapitov, O. V., Artemyev, A. V., & Zhang, X. J. (2019). Impact of significant time-integrated geomagnetic activity on 2-MeV electron flux. *Journal of Geophysical Research (Space Physics)*, *124*(6), 4445–4461. https://doi.org/10.1029/2019JA026659

Mourenas, D., Agapitov, O. V., Artemyev, A. V., & Zhang, X. J. (2022). A climatology of long-duration high 2-MeV electron flux periods in the outer radiation belt. *Journal of Geophysical Research (Space Physics)*, *127*(8), e30661. https://doi.org/10.1029/2022JA030661

Mourenas, D., Artemyev, A. V., Zhang, X. J., & Angelopoulos, V. (2022). Extreme energy spectra of relativistic electron flux in the outer radiation belt. *Journal of Geophysical Research (Space Physics)*, *127*(11), e2022JA031038. https://doi.org/10.1029/2022JA031038

Mourenas, D., Artemyev, A. V., Zhang, X. J., & Angelopoulos, V. (2023). Upper limit on outer radiation belt electron flux based on dynamical equilibrium. *Journal of Geophysical Research (Space Physics)*, *128*(8), e2023JA031676. https://doi.org/10.1029/2023JA031676

Mourenas, D., Artemyev, A. V., Zhang, X. J., & Angelopoulos, V. (2024). Checking key assumptions of the Kennel-Petschek flux limit with ELFIN CubeSats. *Journal of Geophysical Research (Space Physics)*, *129*(2), e2023JA032193. https://doi.org/10.1029/2023JA032193

Mourenas, D., Artemyev, A. V., Zhang, X.-J., Angelopoulos, V., Tsai, E., & Wilkins, C. (2021). Electron lifetimes and diffusion rates inferred from ELFIN measurements at low altitude: First results. *Journal of Geophysical Research: Space Physics*, *126*(11), e2021JA029757. https://doi.org/10.1029/2021JA029757

Mourenas, D., Zhang, X.-J., Artemyev, A. V., Angelopoulos, V., Thorne, R. M., Bortnik, J., et al. (2018). Electron nonlinear resonant interaction with short and intense parallel chorus wave packets. *J. Geophys. Res. (Space Physics)*, *123*(6), 4979–4999. https://doi.org/10.1029/2018JA025417

Mourenas, D., Zhang, X. J., Nunn, D., Artemyev, A. V., Angelopoulos, V., Tsai, E., & Wilkins, C. (2022). Short chorus wave packets: Generation within chorus elements, statistics, and consequences on energetic electron precipitation. *Journal of Geophysical Research (Space Physics)*, *127*(5), e30310. https://doi.org/10.1029/2022JA030310

O'Brien, T. P., & Moldwin, M. B. (2003). Empirical plasmapause models from magnetic indices. *Geophysical Research Letters*, *30*(4), 1152. https://doi.org/10.1029/2002GL016007

Olifer, L., Mann, I. R., Claudepierre, S. G., Baker, D. N., Spence, H. E., & Ozeke, L. G. (2022). A natural limit to the spectral hardness of worst case electron radiation in the terrestrial van allen belt. *J. Geophys. Res. (Space Physics)*, *127*(8), e2022JA030506. https://doi.org/10.1029/2022JA030506

Olifer, L., Mann, I. R., Kale, A., Mauk, B. H., Claudepierre, S. G., Baker, D. N., et al. (2021). A tale of two radiation belts: The energy-dependence of self-limiting electron space radiation. *Geophysical Research Letters*, *48*(20), e95779. https://doi.org/10.1029/2021GL095779

Olifer, L., Mann, I. R., Ozeke, L. G., Walton, S. D., Breneman, A. W., & Murphy, K. (2023). Intense energetic electron precipitation caused by the self-limiting of space radiation. *Geophysical Research Letters*, *50*(21), e2023GL105392. https://doi.org/10.1029/2023GL105392

Omura, Y., Katoh, Y., & Summers, D. (2008). Theory and simulation of the generation of whistler-mode chorus. *J. Geophys. Res. (Space Physics)*, *113*(A4), 4223. https://doi.org/10.1029/2007JA012622

Omura, Y., & Nunn, D. (2011). Triggering process of whistler mode chorus emissions in the magnetosphere. *J. Geophys. Res. (Space Physics)*, *116*(A5), A05205. https://doi.org/10.1029/2010JA016280

Ozeke, L. G., Mann, I. R., Olifer, L., Chakraborty, S., & Pettit, J. M. (2024). The relationship between electron precipitation and the population of trapped electrons in LEO: New evidence supporting a natural limit to the flux of energetic electrons. *J. Geophys. Res. (Space Physics)*, *129*(5), e2023JA031964. https://doi.org/10.1029/2023JA031964

Press, W. H., Teukolsky, S. A., Vetterling, W. T., & Flannery, B. P. (1992). Numerical recipes in FORTRAN. The art of scientific computing.

Saint-Girons, E., Zhang, X.-J., Mourenas, D., Artemyev, A. V., & Angelopoulos, V. (2024). Omnidirectional energetic electron fluxes from 150 to 20,000 km: An ELFIN-based model. *J. Geophys. Res. (Space Physics)*, *129*(10), e2024JA032977. https://doi.org/10.1029/2024JA032977

Schulz, M. (1974). Particle saturation of the outer zone: A nonlinear model. *Astrophysics and Space Science*, *29*(1), 233–242. https://doi.org/10.1007/BF00642726

Schulz, M., & Davidson, G. T. (1988). Limiting energy spectrum of a saturated radiation belt. *J. Geophys. Res. (Space Physics)*, *93*(A1), 59–76. https://doi.org/10.1029/JA093iA01p00059

Selesnick, R. S., Looper, M. D., & Albert, J. M. (2004). Low-altitude distribution of radiation belt electrons. *Journal of Geophysical Research (Space Physics)*, *109*(A11), A11209. https://doi.org/10.1029/2004JA010611

Shane, A. D., Marshall, R. A., Claudepierre, S. G., & Pettit, J.-M. (2023). Electron lifetimes measured at LEO: Comparison with RBSP estimates and pitch angle resolved lifetimes. *J. Geophys. Res. (Space Physics)*, *128*(8), e2023JA031679. https://doi.org/10.1029/2023JA031679

Summers, D., Omura, Y., Miyashita, Y., & Lee, D.-H. (2012). Nonlinear spatiotemporal evolution of whistler mode chorus waves in Earth's inner magnetosphere. *J. Geophys. Res. (Space Physics)*, *117*(A9), 9206. https://doi.org/10.1029/2012JA017842

Summers, D., & Shi, R. (2014). Limiting energy spectrum of an electron radiation belt. *J. Geophys. Res. (Space Physics)*, *119*(8), 6313–6326. https://doi.org/10.1002/2014JA020250

Summers, D., & Stone, S. (2022). Analysis of radiation belt killer electron energy spectra. *J. Geophys. Res. (Space Physics)*, *127*(9), e2022JA030698. https://doi.org/10.1029/2022JA030698

Summers, D., Tang, R., & Thorne, R. M. (2009). Limit on stably trapped particle fluxes in planetary magnetospheres. *J. Geophys. Res. (Space Physics)*, *114*(A10), 10210. https://doi.org/10.1029/2009JA014428

Tao, X., Zonca, F., & Chen, L. (2017). Identify the nonlinear wave-particle interaction regime in rising tone chorus generation. *Geophysical Research Letters*, *44*(8), 3441–3446. https://doi.org/10.1002/2017GL072624

Thorne, R. M., O'Brien, T. P., Shprits, Y. Y., Summers, D., & Horne, R. B. (2005). Timescale for MeV electron microburst loss during geomagnetic storms. *J. Geophys. Res. (Space Physics)*, *110*(A9), 9202. https://doi.org/10.1029/2004JA010882

Tsai, E., Artemyev, A., Ma, Q., Mourenas, D., Agapitov, O., Zhang, X.-J., & Angelopoulos, V. (2024). Key factors determining nightside energetic electron losses driven by whistler-mode waves. *J. Geophys. Res. (Space Physics)*, *129*(3), e2023JA032351. https://doi.org/10.1029/2023JA032351

Tsurutani, B. T., & Smith, E. J. (1977). Two types of magnetospheric ELF chorus and their substorm dependences. *J. Geophys. Res. (Space Physics)*, *82*(32), 5112–5128. https://doi.org/10.1029/JA082i032p05112

Walton, S. D., Mann, I. R., Olifer, L., Ozeke, L. G., Forsyth, C., Rae, I. J., et al. (2023). The response of electron pitch angle distributions to the upper limit on stably trapped particles. *J. Geophys. Res. (Space Physics)*, *128*(11), e2023JA031988. https://doi.org/10.1029/2023JA031988

Zhang, X. J., Agapitov, O., Artemyev, A. V., Mourenas, D., Angelopoulos, V., Kurth, W. S., et al. (2020). Phase decoherence within intense chorus wave packets constrains the efficiency of nonlinear resonant electron acceleration. *Geophysical Research Letters*, *47*(20), e89807. https://doi.org/10.1029/2020GL089807